Science for Energy and Environment
https://www.sciltp.com/journals/see

Article

Spatiotemporal Evolution and Expansion Potential of the Reaction Zone in a Solar-Driven Biomass Pyrolysis Reactor Packed with SiC Foam

Yang Liu [1], Ruming Pan [2,*], Renaud Ansart [3] and Gérald Debenest [1,*]

[1] Univ Toulouse, Toulouse INP, CNRS, IMFT, 31400 Toulouse, France
[2] School of Energy Science and Engineering, Harbin Institute of Technology, Harbin 150001, China
[3] Univ Toulouse, Toulouse INP, CNRS, LGC, 31400 Toulouse, France
* Correspondence: ruming.pan@hit.edu.cn (R.P.); gerald.debenest@toulouse-inp.fr (G.D.)

How To Cite: Liu, Y.; Pan, R.; Ansart, R.; et al. Spatiotemporal Evolution and Expansion Potential of the Reaction Zone in a Solar-Driven Biomass Pyrolysis Reactor Packed with SiC Foam. *Science for Energy and Environment* **2026**, *3*(2), 7. https://doi.org/10.53941/see.2026.100007

Received: 27 May 2026
Revised: 23 Jun 2026
Accepted: 29 Jun 2026
Published: 1 July 2026

Abstract: This study performed a CFD-based analysis to assess the reaction-region expansion potential of a solar-driven biomass pyrolysis reactor packed with SiC foam. Reacted volume fraction (*RVF*), temperature volume fraction (*TVF*), and the operational conversion front defined by the 700 K isotherm were used to quantify the formation and propagation of the effective reaction region. The results show that the operational conversion front in the SiC foam reactor continued to propagate toward the unreacted region without apparent stagnation. The available time window for further front propagation was approximately five times larger than the time required to cover the remaining unreacted region near the original bed. Moreover, under a conservative assumption for a 12.5% reactor extension, the required finite axial temperature gradient was about two orders of magnitude larger than the local axial temperature gradient at the original bed end. These results indicate that the expanded reaction region can compensate for the feedstock loading capacity loss caused by the SiC foam skeleton, while the reactor still retains further expansion potential.

Keywords: solar-driven pyrolysis; biomass; SiC foam; reaction zone expansion; conversion front; CFD

1. Introduction

In the context of low-carbon energy transition, biomass is a renewable carbon source that can be converted into fuels, heat, and chemicals through thermochemical processes [1]. Solar-driven biomass thermochemical conversion combines a low-carbon heat source with a carbon-neutral feedstock, thereby reducing the dependence on external fossil energy input [2,3]. Therefore, solar biomass pyrolysis provides a promising pathway for renewable energy utilization and carbon resource conversion [3].

Various reactor configurations have been developed for solar thermochemical conversion, including spouted beds, vortex beds, fluidized beds, molten-salt reactors, and packed beds [4,5]. These reactors usually involve trade-offs among heat transfer efficiency, structural complexity, operating cost, and maintenance requirements [6,7]. Reactors with high thermal efficiency are often associated with more complex designs, additional auxiliary systems, and higher cost-related constraints [8,9]. In contrast, packed-bed reactors have simple structures, low costs, and convenient operation, but they usually suffer from weak internal heat transfer and strong temperature non-uniformity, which limit the effective utilization of the reactor bed volume [3,10].

Current studies on solar-driven fixed-bed thermochemical reactors mainly focus on performance improvement within fixed-volume and small-scale reactors [11]. Most previous evaluations are based on the temperature field, product yield, or conversion degree within the existing reactor volume [12,13]. However, whether the effective reaction region can be correspondingly expanded during reactor scale-up remains insufficiently explored [4,14]. Clarifying this question is important for evaluating the scale-up potential of laboratory-scale solar thermochemical reactors toward industrial application [15].

In our previous study, silicon carbide (SiC) foam was introduced into a packed-bed reactor to improve internal heat transfer and reduce temperature gradients [16,17]. The results showed that the continuous conductive skeleton of SiC foam can significantly enhance heat transfer within the reaction bed and facilitate the formation of the effective reaction region. However, the solid skeleton of SiC foam occupies part of the space that would otherwise be available for biomass loading [17]. Previous analyses showed that some cases with favorable thermal behavior did not achieve high overall effective conversion because lower foam porosity reduced the actual feedstock loading capacity [16,17]. Therefore, the key issue for SiC foam reactors is not only whether the effective reaction region can be improved within the current geometry, but also whether the improved region can be further expanded to compensate for the loading loss caused by foam addition.

Based on this issue, this study evaluates the expandability of the effective reaction region in a solar-driven biomass pyrolysis reactor packed with SiC foam. First, reacted volume fraction (*RVF*) and temperature volume fraction (*TVF*) are introduced to quantify the formation of the effective reaction region, and the reactor performances is compared between the no-foam case (NF) and the foam-present case (YF). Then, the 700 K isotherm is used to define the operational conversion front, and its propagation is analyzed through the front penetration depth and propagation velocity. Finally, the temperature field near the potential extension region and axial heat-transfer indicators are used to assess whether a 12.5% reactor bed extension can compensate for the feedstock loading capacity loss caused by the SiC foam skeleton. Through this analysis, this study aims to clarify the effective reaction-region expandability of the SiC foam packed-bed reactor under the present heat input level and to provide a basis for further scale-up analysis of solar-driven packed-bed reactors.

2. Methodology

2.1. Reactor Configuration and Numerical Model

The reactor configuration used in this study was based on the prototype reported by Piatkowski et al. [18]. As shown in Figure 1, the reactor mainly consists of a top graphite emitter plate, a packed bed, SiC side walls, and an external insulation layer. The graphite emitter plate absorbs the concentrated solar radiation and transfers heat downward to the packed bed mainly by radiation. The carrier gas enters from the bottom of the packed bed, mixes with the pyrolysis products, and exits from the top of the bed. The reactor has an inner diameter of 143 mm and a height of 160 mm. The packed bed occupies half of the reactor height.

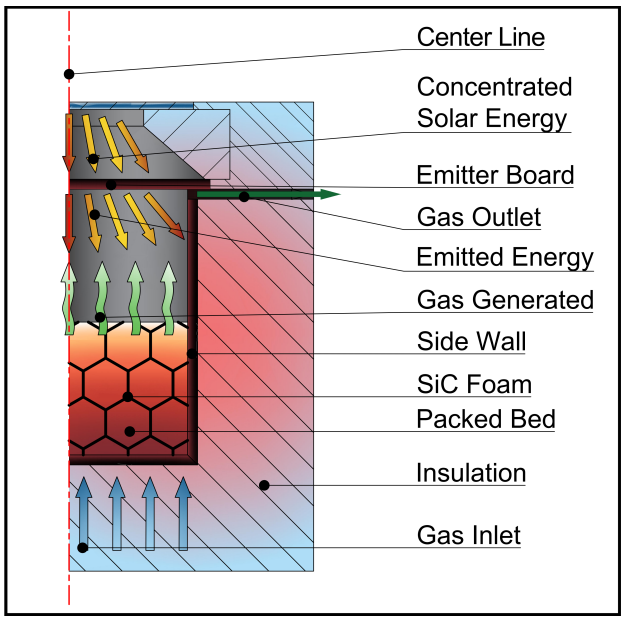

Figure 1. Schematic of the 2D axisymmetric SiC foam packed-bed reactor model for solar-driven biomass pyrolysis.

Beech chips were selected as the feedstock, and nitrogen was used as the carrier gas. The nominal residence time was defined as the ratio between the original reaction volume and the inlet volumetric flow rate of nitrogen under the inlet condition. In this study, the nominal residence time was set to 60 s. The SiC foam has a porosity of 0.9 and a pore diameter of 2 mm. Based on our previous study [19], the solar input power was set to 3.2 kW, which is within a suitable range to reach the reaction threshold without causing excessive overheating. The prescribed heating time was 1200 s.

The numerical simulations were performed using COMSOL Multiphysics 6.2. The geometry was simplified as a two-dimensional axisymmetric model. The reaction kinetic model consisted of the biomass pyrolysis mechanism proposed by Debiagi et al. [20] and the oil cracking mechanism reported by Lao et al. [21]. In total, a semi-detailed kinetic model including 54 reactions was used. The governing equations, boundary conditions, and numerical procedures were described in detail in our previous study [19].

2.2. Definition of Evaluation Indicators

The local solid conversion $C(\mathbf{x}, t)$ at position $\mathbf{x}$ and time t is defined as:

$$C(\mathbf{x}, t) = 1 - \frac{\rho_{\text{residue}}(\mathbf{x}, t)}{\rho_0} \tag{1}$$

where $\rho_{\text{residue}}(\mathbf{x},t)$ is the local residue density, and ρ_0 is the initial solid density.

The reacted volume fraction (*RVF*) is defined as the fraction of the reactor bed volume where the local solid conversion exceeds a prescribed conversion threshold:

$$RVF(t) = \frac{1}{V_{\text{R}}} \iiint_0^{V_{\text{R}}} H(C(\mathbf{x}, t) - C_{\text{th}}) dV \tag{2}$$

where V_{R} is the reactor bed volume, and C_{th} is the conversion threshold. In this study, C_{th} is set to 70%. $H(\cdot)$ is the Heaviside function used to identify whether a local volume element reaches the prescribed conversion threshold:

$$H(\xi) = \begin{cases} 1, \xi \geq 0 \\ 0, \xi < 0 \end{cases} \tag{3}$$

where ξ is the threshold-based argument of the Heaviside function. A non-negative value of ξ indicates that the prescribed criterion is satisfied, and the corresponding local volume element is counted in the integral.

The temperature volume fraction (*TVF*) is defined as the fraction of the reactor bed volume where the local temperature exceeds a prescribed temperature threshold:

$$TVF(t) = \frac{1}{V_{\text{R}}} \iiint_0^{V_{\text{R}}} H(T(\mathbf{x}, t) - T_{\text{th}}) dV \tag{4}$$

where T_{th} is the temperature threshold. In this study, T_{th} is set to 700 K.

3. Results and Discussion

3.1. Reactor Comparison

Here, the No Foam (NF) and Yes Foam (YF) cases refer to the reactor configurations without and with SiC foam, respectively. Figure 2a compares the axial temperature profiles of the NF and YF cases at the end of heating. In the NF case, the temperature remains concentrated near the upper part of the bed, and the lower part of the bed is still insufficiently heated at 1200 s. In contrast, the YF case shows a smoother axial temperature profile and a slower temperature decrease along the bed depth. This comparison indicates that the continuous SiC foam skeleton enhances axial heat transfer and promotes heat penetration into the deeper region of the packed bed. This behavior is consistent with previous studies [16,17,19].

Figure 2b compares the temporal evolutions of *RVF* and *TVF* in the NF and YF cases, where C_{th} = 70% and T_{th} = 700 K are used to define the effective conversion and temperature volumes, respectively. In the NF case, *RVF* reaches only 53% by the end of the heating period, and *TVF* shows a similar final level. In contrast, in the YF case, both *RVF* and *TVF* reach 100% at 915 s. This comparison indicates that the introduction of SiC foam significantly enhances heat transfer and enables the complete formation of the effective reaction region within the prescribed reaction time.

This result also determines the scope of the following expansion analysis. At the end of the reaction, nearly half of the NF bed volume remains outside the effective reaction region. Therefore, the NF case has not yet fully utilized the original bed volume, and further discussion of its downward expansion potential

within the prescribed reaction time is not physically meaningful. For this reason, the following analysis of reaction-zone expansion focuses on the YF case.

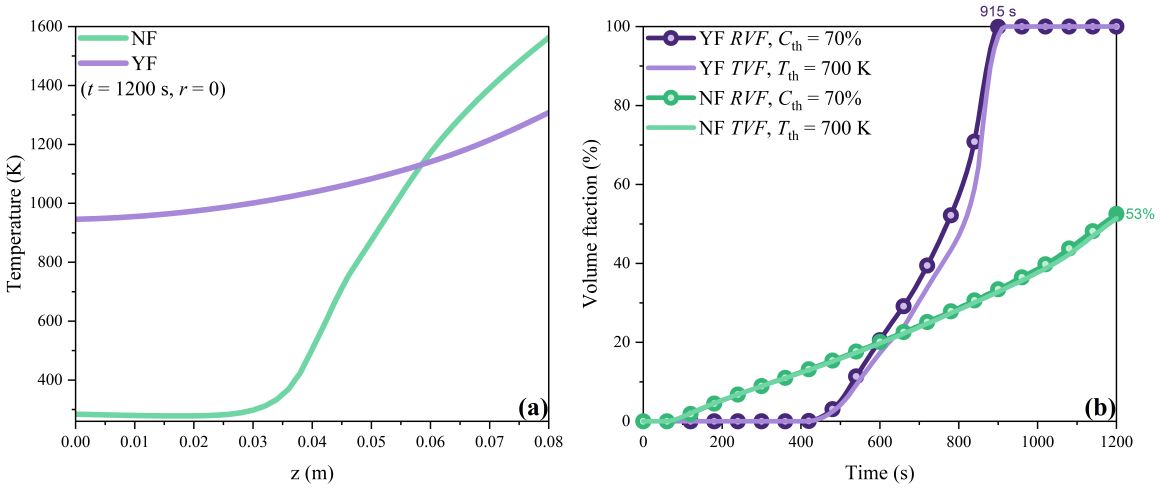

Figure 2. (**a**) Axial temperature profiles for the NF and YF cases at the end of the heating; (**b**) temporal evolutions of *RVF* and *TVF* in the NF and YF cases with C_{th} = 70% and T_{th} = 700 K.

In both cases, the *RVF* and *TVF* curves almost overlap throughout the reaction. This agreement suggests that, at each time, the volume reaching T_{th} = 700 K is nearly identical to the volume reaching C_{th} = 70%. This temperature-conversion correspondence is also consistent with the thermogravimetric observations reported in the literature, where biomass pyrolysis generally approaches completion at around 700 K and the final solid residue is approximately 30% of the initial mass [22,23]. Accordingly, in the following sections, the 700 K isotherm is used to define the operational conversion front.

3.2. Downward Propagation Potential of the Conversion Front

Table 1 summarizes the key time points during the downward propagation of the operational conversion front in the YF case. Figure 3 further shows the temporal evolution of this front, which is defined by the 700 K isotherm. The front first appears at 413 s and then propagates downward mainly along the axial direction. It reaches z = 0.01 m along the z-axis at 850 s, loses its intersection with the z-axis at 853 s, and exits the reactor domain at 915 s. Overall, the front propagates relatively slowly before 800 s, whereas a much faster downward movement is observed after 800 s. This indicates that the lower part of the reactor rapidly crosses the 700 K threshold during the later stage of heating.

Table 1. Key time points related to the downward propagation of the operational conversion front in the YF reactor.

Event	Symbol	Time
Onset of the operational conversion front	t_{onset}	413 s
Arrival at z = 0.01 m along the z-axis	$t_{z,0.01}$	850 s
Loss of intersection with the z-axis	t_{off}	853 s
Exit from the reactor domain	t_{out}	915 s
End of the prescribed heating period	t_{end}	1200 s

Figure 3 also shows that the evolution of the 700 K front is mainly governed by axial downward propagation. At the same time, the front generally reaches its deepest position near the z-axis, indicating that the z-axis corresponds to the leading path of downward front propagation. Therefore, the front position along the z-axis is used to evaluate whether the conversion front still has the potential to propagate further downward near the lower boundary of the reactor.

To quantify this process, Figure 4 presents the front penetration depth $z_f(t)$ and the front propagation velocity $v_f(t)$ along the z-axis. Here, $z_f(t)$ is defined as the deepest position reached by the 700 K front on the z-axis at time t. Since downward propagation corresponds to a decrease in $z_f(t)$, the front propagation velocity is defined as:

$$v_f(t) = -\frac{dz_f(t)}{dt} \quad (5)$$

With this definition, a positive value of v_f (t) indicates downward movement of the front. If v_f (t) remains positive when the front approaches the lower boundary of the reactor, the front has not stagnated near the current geometric boundary. Therefore, v_f (t) can be used as a direct indicator of the remaining downward propagation potential.

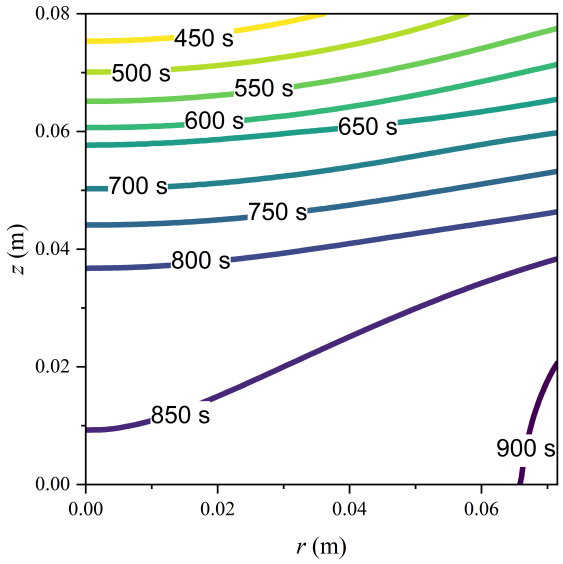

Figure 3. Temporal evolution of the operational conversion front in the YF reactor.

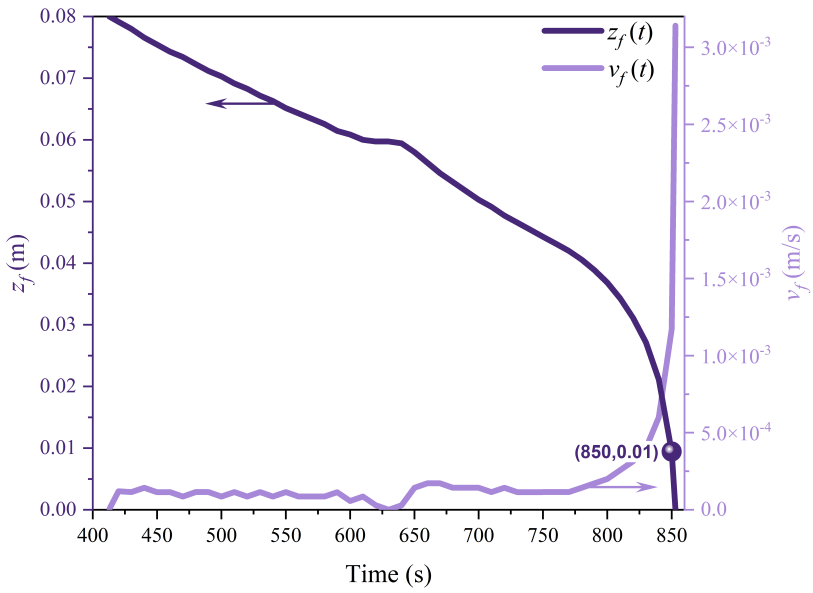

Figure 4. Penetration depth and propagation velocity of the operational conversion front along the z-axis.

As shown in Figure 4, before 800 s, z_f (t) decreases almost linearly, and v_f (t) remains relatively stable at approximately 1.15×10^{-4} m·s^{-1}. This indicates that the front propagates downward at a nearly constant rate during this stage. After 800 s, z_f (t) decreases much more rapidly, and v_f (t) increases sharply before the front loses its intersection with the z-axis. This behavior is consistent with the increased spacing between the front contours after 800 s in Figure 3, indicating that a large lower region of the reactor rapidly crosses the 700 K threshold during the later stage. It should be noted that the peak value of v_f (t) may be affected by numerical differentiation of discrete data; therefore, its absolute value should not be overinterpreted. However, the positive and increasing trend of v_f (t) still indicates that the front does not exhibit stagnation near the lower boundary.

Overall, the 700 K front does not show obvious attenuation when it approaches the lower boundary of the reactor. Instead, both z_f (t) and v_f (t) indicate that the operational conversion front maintains a clear downward propagation trend near the current geometric boundary. This result suggests that the YF reactor still has the potential for further downward expansion of the effective reaction region.

3.3. Feasibility of Reaction-Region Extension

The presence of SiC foam reduces the volume available for feedstock loading because part of the reactor volume is occupied by the solid foam skeleton. If the reactor can be extended downward, the additional volume may compensate for this loss of feedstock loading capacity. In the present YF case, the porosity of the SiC foam is 0.9. Based on the current bed height of 0.08 m, compensating for the feedstock loading loss caused by the foam skeleton requires an additional height of approximately 0.009 m. Hence, an additional thickness of 0.01 m is considered in this study, which corresponds to a 12.5% extension relative to the original bed volume. The following analysis evaluates whether the operational conversion front can penetrate the extended region of [−0.01, 0] m.

To provide a reference, the thermal behavior of the current bottom region [0, 0.01] m is first analyzed after the arrival of the front. Figure 5 shows the temperature contours in this region at $t_{z,0.01}$ = 850 s, t_{out} = 915 s, and t_{end} = 1200 s. The temperature difference within this region remains around 60 K at these three moments, indicating that no severe temperature non-uniformity occurs near the reactor bottom. According to Table 1, the time required for the front to cover the bottom region from z = 0.01 m to the reactor boundary is: $t_{cover} = t_{out} - t_{z,0.01}$ = 65 s. The available time window for the front to enter the extended region after losing its intersection with the z-axis is: $t_{window} = t_{end} - t_{off}$ = 347 s. Thus, t_{window} is approximately five times larger than t_{cover}. This comparison indicates that the available heating duration is sufficient for the front to penetrate an additional 0.01 m thickness.

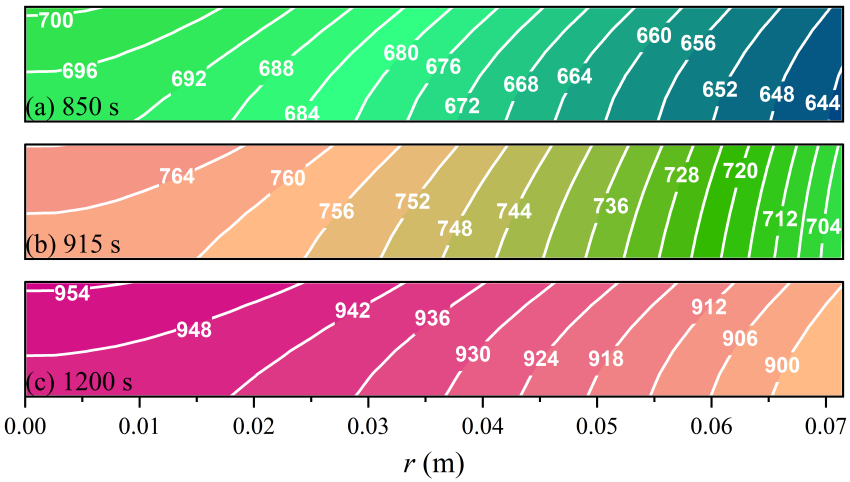

Figure 5. Temperature contours in the bottom region of the reactor ($z \in [0, 0.01]$ m) at (**a**) 850 s, (**b**) 915 s, and (**c**) 1200 s.

Figure 5c further shows that, at t = 1200 s, the temperature in the current bottom region is generally higher than 900 K, which is far above the 700 K criterion used to define the operational conversion front. This indicates that a large thermal margin remains near the lower boundary of the reactor at the end of the heating period.

To further assess whether the extended region can reach 700 K, Figure 6a presents the temperature distribution at z = 0 m at t = 1200 s. If the temperature at z = −0.01 m is conservatively assumed to be only 700 K at the same time, the finite axial temperature gradient between z = 0 and z = −0.01 m can be estimated as $|\Delta T/\Delta z|$, as shown in Figure 6b. Its value ranges from 1.9 × 10^4 to 2.5 × 10^4 K·m^{-1}. By comparison, the local axial temperature gradient $|\partial T/\partial z|$ at z = 0 m ranges only from 150 to 550 K·m^{-1}. The finite axial temperature gradient required to maintain this conservative assumption is therefore about two orders of magnitude larger than the local axial temperature gradient at the current lower boundary. Considering the axial continuity of the SiC foam skeleton, this assumption is overly conservative. Therefore, the actual temperature at z = −0.01 m is expected to be higher than 700 K.

Overall, the YF reactor still shows a clear potential for downward heat transfer and front propagation near the current lower boundary. The time-scale analysis indicates that the remaining heating window is sufficient for the operational conversion front to penetrate the additional 0.01 m region, corresponding to the 12.5% extension. The temperature-field and finite axial temperature gradient analyses further support the feasibility of reaching the 700 K criterion in the extended region. Therefore, for the SiC foam reactor with a porosity of 0.9, a 12.5% extension of the effective reaction region is theoretically feasible and can

compensate for the loss of feedstock loading capacity caused by the solid foam skeleton, while the reactor still retains further expansion potential.

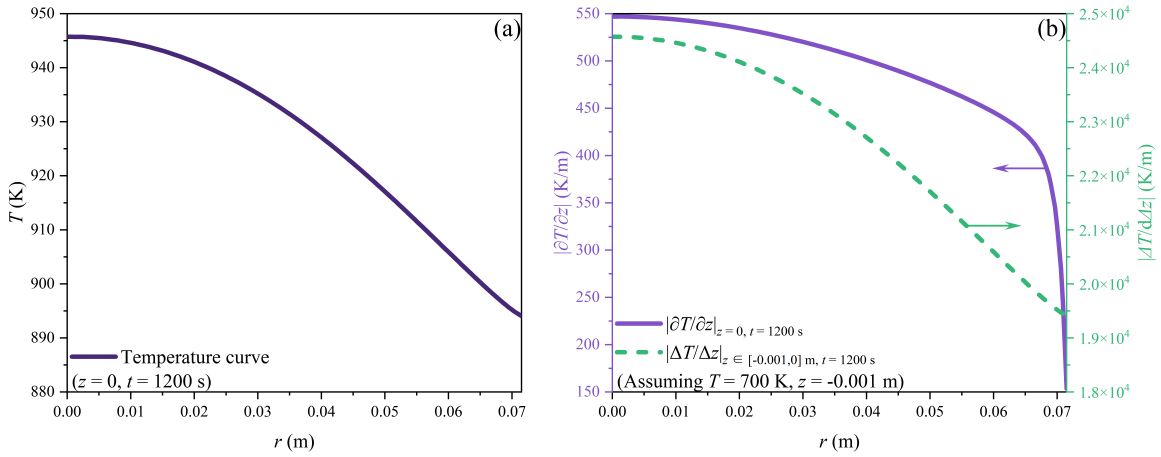

Figure 6. (**a**) Radial temperature profile at z = 0 m and t = 1200 s; (**b**) local axial temperature gradient at z = 0 m and finite axial temperature gradient estimated between z = 0 and z = −0.01 m, assuming T = 700 K at z = −0.01 m.

Although the present analysis supports the feasibility of reactor extension, explicit simulations using an extended reactor geometry will be necessary in future work to quantify the actual front propagation dynamics and conversion efficiency in the enlarged domain.

From an engineering perspective, the cost and availability of the foam material should also be considered for reactor scale-up. Although SiC foam provides high thermal stability and good radiative/thermal transport properties, its cost may limit large-scale application. Therefore, cheaper conductive porous materials, such as metallic foams or metallic curls generated during machining processes, could be considered as potential alternatives. These materials are widely available and generally have higher thermal conductivity than ceramic foams. However, their thermal stability, oxidation resistance, compatibility with biomass pyrolysis environments, and long-term structural durability should be further evaluated before practical implementation.

4. Conclusions

This study evaluated the reaction region expansion potential of a solar-driven biomass pyrolysis reactor packed with SiC foam. The simulations were conducted with a SiC foam porosity of 0.9, a solar input power of 3.2 kW, and a prescribed heating time of 1200 s. A local conversion of 70% and a temperature of 700 K were used as the criteria for effective pyrolysis completion.

The comparison between the No Foam (NF) and Yes Foam (YF) cases showed that SiC foam significantly improved the formation of the effective reaction region. In the NF case, the reacted volume fraction (*RVF*) reached only 53% by the end of the heating period, and the temperature volume fraction (*TVF*) showed a similar final level. In contrast, in the YF case, both *RVF* and *TVF* reached 100% at 915 s. The close overlap between *RVF* and *TVF* in both cases supports the use of the 700 K isotherm to define the operational conversion front.

The propagation analysis showed that the 700 K front did not stagnate near the lower boundary of the YF reactor. After 800 s, the front penetration depth z_f (t) decreased rapidly, while the front propagation velocity v_f (t) increased markedly, indicating a clear downward propagation tendency near the current reactor boundary.

The feasibility of a 12.5% reaction region extension, corresponding to an additional 0.01 m thickness, was supported by the time-scale and thermal analyses. The available time window for front propagation was approximately five times larger than the time required to cover the current bottom region. In addition, the finite axial temperature gradient required to maintain 700 K at z = −0.01 m was about two orders of magnitude higher than the local axial temperature gradient at z = 0 m, indicating that this assumption was overly conservative.

Overall, the SiC foam reactor with a porosity of 0.9 shows clear potential for downward expansion. A 12.5% reaction region extension is theoretically feasible and can compensate for the feedstock loading capacity loss caused by the solid foam skeleton, while the remaining expansion potential provides a basis

for larger-scale reactor design. Future work may examine cheaper conductive alternatives, such as metallic foams or machining-derived metallic curls, for practical reactor scale-up, provided that their thermal stability and compatibility are confirmed.

Author Contributions

Y.L.: conceptualization, methodology, software, validation, formal analysis, investigation, data curation, visualization, writing—original draft preparation. R.P.: conceptualization, methodology, writing—review and editing, supervision. R.A.: methodology, writing—review and editing, supervision. G.D.: methodology, writing—review and editing, supervision, project administration, funding acquisition. All authors have read and agreed to the published version of the manuscript.

Funding

This work was supported by the Institut Carnot ISIFoR through the 2025 program plume; National Key R&D Program of China (No. 2024YFE0116800); National Natural Science Foundations of China (No. 52506076); Natural Science Foundation of Heilongjiang Province, China (No. LH2024E040); Fundamental Research Funds for the Central Universities (No. HIT.NSFJG202424).

Data Availability Statement

The data presented in this study are available from the corresponding author upon reasonable request.

Conflicts of Interest

The authors declare no conflict of interest.

Use of AI and AI-Assisted Technologies

During the preparation of this work, the authors used ChatGPT to assist with language polishing. After using this tool, the authors reviewed and edited the content as needed and take full responsibility for the content of the published article.

References

1. El-Fawal, E.M.; El Naggar, A.M.A.; El-Zahhar, A.A.; et al. Biofuel production from waste residuals: Comprehensive insights into biomass conversion technologies and engineered biochar applications. *RSC Adv.* **2025**, *15*, 11942–11974. https://doi.org/10.1039/D5RA00857C.
2. Pan, H.; Li, J.; Wang, Y.; et al. Solar-driven biomass reforming for hydrogen generation: Principles, advances, and challenges. *Adv. Sci.* **2024**, *11*, 2402651. https://doi.org/10.1002/advs.202402651.
3. Makkawi, Y.; Ibrahim, M.; Yasir, N.; et al. Solar-thermal conversion of biomass: Principles of solar concentrators/reactors, reported studies, and prospects for large-scale implementation. *Fuel Process. Technol.* **2024**, *264*, 108139. https://doi.org/10.1016/j.fuproc.2024.108139.
4. Zhao, J.; Korba, D.; Mishra, A.; et al. Particle-based high-temperature thermochemical energy storage reactors. *Prog. Energy Combust. Sci.* **2024**, *102*, 101143. https://doi.org/10.1016/j.pecs.2024.101143.
5. Bellan, S.; Kodama, T.; Gokon, N.; et al. A review on high-temperature thermochemical heat storage: Particle reactors and materials based on solid–gas reactions. *WIREs Energy Environ.* **2022**, *11*, e440. https://doi.org/10.1002/wene.440.
6. Guo, Y.; Chen, J.; Song, H.; et al. A review of solar thermochemical cycles for fuel production. *Appl. Energy* **2024**, *357*, 122499. https://doi.org/10.1016/j.apenergy.2023.122499.
7. Chen, C.; Jiao, F.; Lu, B.; et al. Challenges and perspectives for solar fuel production from water/carbon dioxide with thermochemical cycles. *Carbon Neutrality* **2023**, *2*, 9. https://doi.org/10.1007/s43979-023-00048-6.
8. Brendelberger, S.; Rosenstiel, A.; Lopez-Roman, A.; et al. Performance analysis of operational strategies for monolithic receiver-reactor arrays in solar thermochemical hydrogen production plants. *Int. J. Hydrogen Energy* **2020**, *45*, 26104–26116. https://doi.org/10.1016/j.ijhydene.2020.06.191.
9. Li, S.; Wheeler, V.M.; Kumar, A.; et al. Thermodynamic guiding principles for designing nonstoichiometric redox materials for solar thermochemical fuel production: Ceria, perovskites, and beyond. *Energy Technol.* **2022**, *10*, 2000925. https://doi.org/10.1002/ente.202000925.
10. Li, L.; Rahbari, A.; Taheri, M.; et al. Experimental evaluation of an indirectly-irradiated packed-bed solar thermochemical reactor for calcination-carbonation chemical looping. *Chem. Eng. J.* **2023**, *468*, 143543. https://doi.org/10.1016/j.cej.2023.143543.

11. Ullah, F.; Hasrat, K.; Mu, M.; et al. Optimizing solar-biomass pyrolysis: Innovations in reactor design and thermal-solar system efficiency. *Energies* **2025**, *18*, 2640. https://doi.org/10.3390/en18102640.
12. Dai, X.; Haussener, S. Non-uniform porous structures and cycling control for optimized fixed-bed solar thermochemical water splitting. *J. Sol. Energy Eng.* **2022**, *144*, 030904. https://doi.org/10.1115/1.4052960.
13. Bulfin, B.; Miranda, M.; Steinfeld, A. Performance indicators for benchmarking solar thermochemical fuel processes and reactors. *Front. Energy Res.* **2021**, *9*, 677980. https://doi.org/10.3389/fenrg.2021.677980.
14. Khan, M.I.; Mishamandani, A.S.; Asfand, F.; et al. Solar driven calcium-looping for thermochemical energy storage system and carbon capture in power and cement industry: A review. *Process Saf. Environ. Prot.* **2025**, *193*, 886–917. https://doi.org/10.1016/j.psep.2024.11.067.
15. Abanades, S.; Rodat, S.; Boujjat, H. Solar thermochemical green fuels production: A review of biomass pyro-gasification, solar reactor concepts and modelling methods. *Energies* **2021**, *14*, 1494. https://doi.org/10.3390/en14051494.
16. Liu, Y.; Pan, R.; Ansart, R.; et al. Numerical simulation of solar-driven biomass gasification by using ceramic foam. *Process Saf. Environ. Prot.* **2024**, *184*, 300–313. https://doi.org/10.1016/j.psep.2024.02.008.
17. Liu, Y.; Pan, R.; Ansart, R.; et al. Optimization and analysis of solar-driven biomass gasification using a CFD-ANN-GA framework. *Energy* **2025**, *325*, 136036. https://doi.org/10.1016/j.energy.2025.136036.
18. Piatkowski, N.; Wieckert, C.; Steinfeld, A. Experimental investigation of a packed-bed solar reactor for the steam-gasification of carbonaceous feedstocks. *Fuel Process. Technol.* **2009**, *90*, 360–366. https://doi.org/10.1016/j.fuproc.2008.10.007.
19. Liu, Y.; Pan, R.; Ansart, R.; et al. Efficient Biomass Pyrolysis under Sub-Design Solar Input through SiC Foam Integration and Process Parameter Tuning. 2026. Available online: https://ssrn.com/abstract=5327617 (accessed on 29 June 2026).
20. Debiagi, P.; Gentile, G.; Cuoci, A.; et al. A predictive model of biochar formation and characterization. *J. Anal. Appl. Pyrolysis* **2018**, *134*, 326–335. https://doi.org/10.1016/j.jaap.2018.06.022.
21. Lao, Z.; Shao, Y.; Gao, X. Multiscale CFD modeling of high-temperature biomass pyrolysis with an intraparticle particle model and detailed pyrolysis kinetics. *Ind. Eng. Chem. Res.* **2022**, *61*, 16843–16856. https://doi.org/10.1021/acs.iecr.2c02992.
22. Brebu, M.; Ioniță, D.; Stoleru, E. Thermal behavior and conversion of agriculture biomass residues by torrefaction and pyrolysis. *Sci. Rep.* **2025**, *15*, 11505. https://doi.org/10.1038/s41598-025-88001-8.
23. Rosero Espín, M.V.; Muñoz Borja, M.A.; Narvaez Cueva, R.A.; et al. Identification and comparison of pyrolysis products of different biomasses from agro-industrial using TGA-FTIR and Py-GC/MS. *Int. J. Renew. Energy Dev.* **2026**, *15*, 305–321. https://doi.org/10.61435/ijred.2026.61812.